Metals and Materials International (2021) 27:4996–5007
https://doi.org/10.1007/s12540-020-00919-y

Effect of Hot Extrusion on Microstructure and Mechanical Properties of Mg–5Sn–xZr Alloys

Omid Sadeddin[1] · Mohammad Moazami-Goudarzi[1] · Mohammad Javad Nayyeri[1]

Received: 9 September 2020 / Accepted: 29 October 2020 / Published online: 30 January 2021

Abstract
The effects of Zr addition (0, 0.5 and 1 wt%) and extrusion ratio (6:1 and 12:1) on microstructure and mechanical properties of the Mg–5Sn alloy were studied. Results showed that the dendritic structure of the as-cast M–5Sn alloy gradually transformed into a nearly globular structure with Zr addition. The effect of Zr addition was evident through refining the microstructure, promoting the tendency to form partially divorced eutectic and increasing the Mg_2Sn volume fraction, which improved the thermal stability of the alloy during homogenizing treatment at high temperatures. Hot extrusion was found to be very effective for enhancing both strength and ductility of the Mg–5Sn–xZr alloys. Grain refinement induced by twin dynamic recrystallization and dynamic precipitation of fine particles were realized as the main strengthening mechanisms of the extruded alloys. It was found that an increase of the extrusion ratio led to relatively coarser grains, lower yield strength, and higher hardening capacities. However, the Mg–5Sn–1Zr alloy extruded with the area-reduction ratio of 12 exhibited the best combination of tensile strength and elongation of 243 MPa and 10.6%, respectively. Moreover, tensile fracture studies revealed the intergranular cracking and quasi-cleavage fracture as the dominant fracture modes of the as-cast and extruded alloys, respectively.

Keywords Mg–Sn–xZr alloys · Extrusion · Microstructure · Grain refinement · Tensile properties

1 Introduction

The increasing need for high strength and lightweight materials has triggered the development of new Mg alloys for structural applications. Owing to offering a good combination of mechanical properties, Mg–Sn based alloys have been of particular interest as the cost-effective heat resistant magnesium alloys in few last years [1, 2]. In comparison with the more commercial Mg–Al and Mg–Zn based alloys, Mg–Sn alloys show a lower tendency to hot tearing and microporosity because of their narrower solidification temperature range [3, 4]. Sn, as the major alloying element, can also improve the corrosion resistance of Mg [5]. However, the most significant advantage of Mg–Sn alloys over currently used Mg–Al based alloys is their superior mechanical properties at high temperatures caused by Mg_2Sn second phase [6]. The high melting point of the intermetallic compound Mg_2Sn (~770 °C) ensures the excellent creep resistance of Mg–Sn alloys. The maximum solid solubility of Sn in Mg is 14.48 wt% at the eutectic temperature of 561 °C, which drops rapidly to 0.17 wt% at room temperature [7, 8]. Therefore, Mg–Sn alloys could be strengthened by precipitation hardening treatment.

Due to the aforementioned properties, Mg–Sn based alloys have strong potentials to be used as a cast or wrought product. However, the production of Mg–Sn alloys using conventional ingot metallurgy results in a Mg matrix with coarse grain sizes and large dendrite arm spacing [9]. Besides, the hardening response of binary Mg–Sn alloys is sluggish because coarse precipitates of Mg_2Sn are directly produced from the supersaturated solid solution [10]. These issues can deteriorate mechanical properties of Mg–Sn alloys. Therefore, there have been extensive researches to improve the mechanical properties of Mg–Sn alloys by adding different alloying

✉ Mohammad Moazami-Goudarzi
moazami@srbiau.ac.ir

Omid Sadeddin
omidsadeddin@yahoo.com

Mohammad Javad Nayyeri
nayyeri.javad@gmail.com

[1] Department of Materials Engineering, Science and Research Branch, Islamic Azad University, Tehran 1477893855, Iran

elements. Elsayed et al. [7] reported the enhanced kinetic of precipitation in the Mg–2.2 at% Sn alloy with Al addition. Zn was also found to increase the age-hardening response of Mg–Sn alloys by changing the Mg_2Sn morphology [11]. Ca addition to the Mg–Sn system results in the formation of CaMgSn and Mg_2Ca phases. These precipitates are thermally more stable than Mg_2Sn, thereby improve the creep resistance of the alloy [12]. Moreover, the effects of other alloying elements such as Li [13], Sr [14], Sb [15], Si [16], rare earth elements [17–20] and misch metals [21] on microstructural modification and mechanical properties of Mg–Sn alloys have also been discussed in the literature.

On the other hand, Mg–Sn based alloys show excellent extrudability [22, 23]. Therefore, high-temperature deformation processes such as hot extrusion can also be employed to further improve mechanical properties of these alloys through eliminating casting defects, grain refinement and precipitation strengthening of particles [17, 24]. Mahallawy et al. [25] achieved a high combination of strength and ductility for the extruded Mg–6Sn–(2–4)Zn alloys. This is mainly due to grain refining, solid solution strengthening and precipitation hardening during extrusion. Zhang et al. [26] studied the effect of extrusion ratio on the microstructure and mechanical properties of as-extruded Mg–6Sn–2Zn–1Ca alloy. Alloys with higher extrusion ratios showed a higher fraction of dynamically recrystallized grains, and consequently, a finer average grain size resulted in improved tensile properties.

Zr is the most efficient grain refiner for Mg alloys. The great potential of Zr as a nucleating agent for Mg is attributed to its hexagonal closed-packed (HCP) crystal structure and lattice parameters close to those of Mg [27]. While Emley et al. [28] reported that the formation of stable compounds with Sn could limit the ability of Zr in grain refining of Sn-containing Mg alloys, there are inconsistent reports in the literature. Pan et al. [29] demonstrated that tensile strength and ductility of the as-cast Mg–3Sn–1Mn alloy were enhanced by the addition of 0.43 wt% Zr, mainly due to the grain refining effect of Zr. Yang et al. [30] also reported that the addition of 0.41–1.18 wt% Zr could effectively refine the grains of Mg–3Sn–2Ca alloys. They concluded that the alloy with 0.76 wt% Zr exhibited the smallest grain size and the best tensile properties at room temperature and 150 °C. However, reports on the effect of Zr addition on binary Mg–Sn alloys are rare. Therefore, this study aims to investigate the effect of Zr addition on microstructure and mechanical properties of the Mg–5Sn alloy in as-cast and extruded conditions. The main focus is on the microstructural changes caused by Zr addition and hot extruding, which affect tensile properties and fracture mechanisms of the alloys.

2 Experimental Procedure

Mg–5 wt% Sn–x wt% Zr (x = 0, 0.5 and 1) alloys were prepared from commercially pure Mg (> 99.9%), pure Sn (> 99.8%) and pure Zr (> 99.5%). Melting was carried out in an electric resistance furnace using a silicon carbide crucible with 115 mm inner diameter and 127 mm height, under the Foseco Magrex 36 covering flux to protect molten magnesium from oxidation. The molten alloys were stirred mechanically at 750 °C for 3 min to ensure chemical homogeneity. The melts were poured into bottom-gating sand molds designed to minimize the melt turbulence during filling, as schematically shown in Fig. 1a.

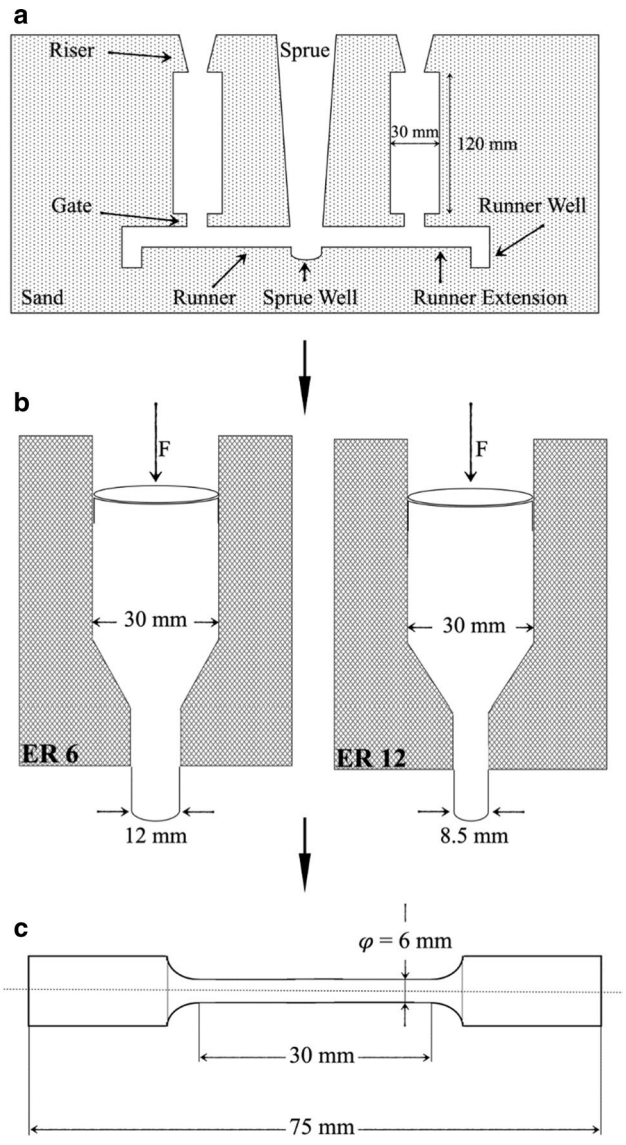

Fig. 1 Schematic illustrations of the **a** sand mold, **b** extrusion and **c** tensile test specimen

The as-cast cylindrical billets were 30 mm in diameter and 120 mm in height. Analyzed compositions of Mg–5Sn–xZr alloys were Mg–5.1 wt%Sn, Mg–4.9 wt%Sn–0.47 wt%Zr and Mg–5.1 wt%Sn–0.92 wt%Zr. The as-cast billets were homogenized at 480 °C for 10 h under a protective argon atmosphere and then water-quenched. Afterward, the homogenized billets were extruded at 400 °C with two different extrusion ratios of 6:1 and 12:1 (denoted as ER6 and ER12, respectively). The ram speed was 5 mm s^{-1}.

Microstructural analysis was carried out using both optical microscopy (OM, Olympus BX51M) and scanning electron microscopy (SEM, FEI ESEM Quanta 200) equipped with energy dispersive spectroscopy (EDS). To minimize the effects of processing parameters such as the cooling rate on the microstructure, central regions of each sample were selected for the microscopic analysis. For the extruded alloys, OM and SEM micrographs were taken from a section normal to the extrusion direction. The surface of specimens was prepared using standard metallographic techniques and then chemically etched with an etchant consisting of 20 ml acetic acid, 6 g picric acid, 40 ml water and 100 ml ethanol. X-ray diffraction (XRD, STOE STADI MP) with monochromatic Cu Kα radiation was used for phase analysis. The grain size was measured by the Heyn linear intercept procedure based on the ASTM E 112 standard.

Hardness measurements were conducted using a Vickers hardness tester (INNOVATEST NEXUS 605U) by applying a load of 98 N for a duration of 15 s. The as-cast and extruded rods were machined into round tensile specimens of 6 mm gauge diameter and 30 mm gauge length. Tensile tests were carried out at room temperature on a tensile testing machine (SANTAM STM-150) with an initial strain rate set at 10^{-3} s^{-1}. The fracture surfaces of tensile specimens were examined by SEM.

3 Results and Discussion

3.1 Microstructure

Optical microstructures of the as-cast Mg–5Sn–xZr alloys are depicted in Fig. 2. The microstructure of all the alloys includes primary α-Mg phase surrounded by a eutectic structure. It can be seen in Fig. 2a that the Mg–5Sn alloy shows a coarse dendritic structure. It is well known that the dendrite arm spacing is inversely proportional to the cooling rate during solidification [31]. Therefore, observation of coarse microstructures in the as-cast condition is mainly due to the relatively low cooling rate normally encountered in the sand casting. In addition, the formation of a coarse dendritic structure can also be attributed to the low value of growth restriction factor (GRF) in the Mg–Sn system. GRF is a parameter that quantifies the effect of segregating solute atoms on the grain size of castings and is expressed as $mC_0(k-1)$, where m is the slope of liquidus line, C_0 is the initial concentration of the solute and k is the equilibrium partition coefficient [32]. The growth rate during dendritic growth is inversely proportional to the GRF value, and consequently, a well-developed coarse dendritic structure is anticipated when the GRF value is low [33]. The observed dendritic configuration is weakened by the addition of 0.5 wt% Zr, and the secondary arms are gradually disappeared in some regions, as exhibited in Fig. 2b. When Sn content increases to 1 wt% (Fig. 2c), many dendritic side arms are disappeared, and a globular structure of α-Mg is formed. The XRD patterns exhibited in Fig. 3 indicate that both binary Mg–5Sn and ternary Mg–5Sn–xZr alloys in the as-cast condition consist of α-Mg and Mg_2Sn phases.

Another microstructural characteristic of Zr containing alloy exhibited in Fig. 2 is their smaller grain size as compared with the binary Mg–5Sn alloy. The average grain size in the as-cast state is found to decrease sharply from 211 to 107 μm by the addition of 1 wt% Zr. The grain refining role of Zr is described by its influence on both nucleation and growth of Mg dendrites/grains. Zr can exist as any three forms of dissolved, undissolved or precipitated particles within the Mg melt. Undissolved and precipitated Zr particles may act as powerful nucleants, helping to produce finer grains. Meanwhile, dissolved Zr can refine the Mg grains by acting as a growth restriction element [34]. During solidification, excess Zr solute atoms segregate at the solid/liquid interface and rapidly build up an effective constitutional undercooling zone ahead of the solidification front.

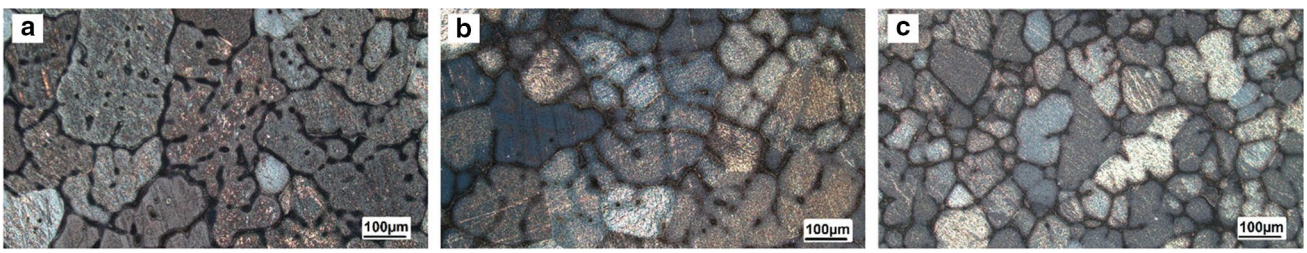

Fig. 2 Optical micrographs of as-cast **a** Mg–5Sn, **b** Mg–5Sn–0.5Zr and **c** Mg–5Sn–1Zr alloys

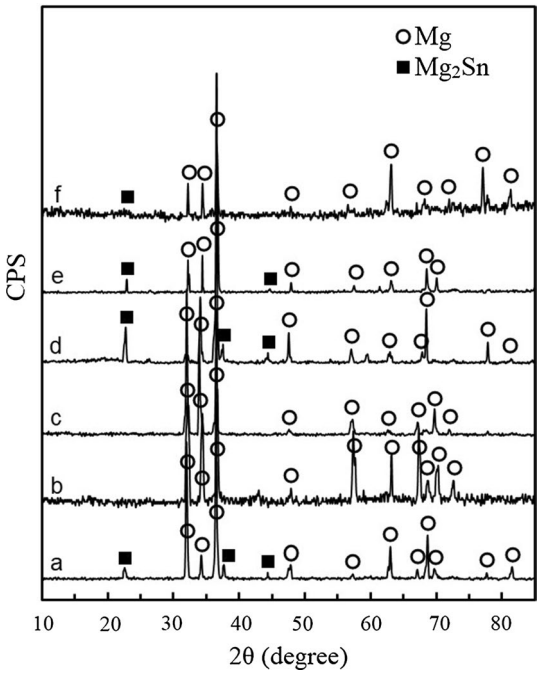

Fig. 3 XRD patterns of **a**, **b**, **c** Mg–5Sn and **d**, **e**, **f** Mg–5Sn–1Zr alloys in **a**, **d** as-cast, **b**, **e** homogenized and **c**, **f** ER6 conditions

Moreover, a high concentration of dissolved atoms can restrict the growth rate of the growing interface [35, 36]. In magnesium, Zr has the highest m(k − 1) value after Fe indicating significant grain refinement potential related to its strong segregating power [37, 38]. The major contribution of Zr in grain refining of Mg alloys is attributed to the dissolved Zr atoms by Qian et al. [39].

To reveal more microstructural details and phases present in the Mg matrix, SEM images of the as-cast alloys are shown in Fig. 4. The results of EDS analysis of different phases are also presented in this figure. Microstructure of the as-cast Mg–5Sn alloy consists of primary α-Mg and eutectic phases, as shown in Fig. 4a. EDS analysis of this alloy indicates that the matrix is a solid solution of Sn in Mg. The second phase is identified as the Mg_2Sn particles by XRD and EDS analysis. Similar to previous reports by other researches [40], the percentage of Mg may be overestimated by quantitative EDS analysis, which can be attributed to the emission of X-ray from the Mg matrix beneath the Mg_2Sn precipitate.

Primary α-Mg is the first phase that forms from the superheated liquid alloy during cooling at liquidus temperature. These α-Mg dendrites contain less Sn solute atom than the initial liquid. The balance of Sn atoms is rejected from the solid phase and accumulates at the solid–liquid interface, forming a solute boundary layer in front of the interface. As the solidification proceeds, this layer is further enriched in solute atoms, which cause diffusive transport of Sn atoms to the liquid bulk. Other growing dendrites gradually restrict the growth of each primary α-Mg phase. As a result, the diffusive transport of Sn atoms is inevitably disrupted before dendrite impingement. This causes a raised Sn concentration above the initial percentage at the lateral border of primary α-Mg phases confirmed by EDS analysis. These Sn-rich regions have appeared as the light gray bands in the backscattered SEM images shown in Fig. 4. Eventually, in the last stage of solidification, the composition of the remainder of the liquid reaches the eutectic composition. Consequently, eutectic solidification takes place at around 561 °C along dendritic/grain boundaries. The eutectic solidification results in the formation of a lamellar structure of α-Mg and Mg_2Sn phase. Mg_2Sn, as an intermetallic compound, is a faceted phase. Therefore, it exhibits an irregular eutectic morphology with a non-faceted metal such as Mg [41]. The formation of lamellar eutectic morphology in Mg is promoted at low cooling rates involved in the sand casting process [42].

It is evident from the magnified SEM image in Fig. 4d that as well as lamellar Mg_2Sn, some precipitates with platelike and globular morphologies are formed. In these cases, there is no cooperative growth of eutectic phases. Mg_2Sn particles may form earlier due to the local enrichment of Sn solute atom and grow individually in a divorced mode between or inside the α-Mg dendrites. While the faceted platelike Mg_2Sn precipitates are only observed at dendritic/grain boundaries, the globular shaped precipitates are distributed at both dendritic/grain boundaries and inside the α-Mg phase, as shown in Fig. 4d. The results of EDS analysis show that the Sn content of platelike precipitates is greater than that of globular Mg_2Sn, indicating the higher Sn segregation at dendrite/grain boundaries.

In Zr containing alloys, dissolution of both Sn and Zr atoms in the α-Mg has created a ternary solid solution as the matrix, confirmed by EDS analysis. Another microstructural characteristic of Mg–5Sn–xZr alloys, as exhibited in Fig. 4d, e, f, is the presence of partially divorced eutectic structure where islands of α-Mg within the Mg_2Sn phase are revealed. It can be observed that the tendency to form partially divorced eutectic morphology increases with Zr addition. It seems that the segregation of Zr atoms around the growing Mg_2Sn particles changes their surface energy, leading to the growth of eutectic constituents in a partially divorced manner. The effects of alloy composition and cooling conditions on the eutectic morphology of Mg alloys have been described in detail by Dahle et al. [42].

Mg and Zr have not been observed to form any intermetallic compounds. Meanwhile, according to the binary Sn–Zr phase diagram, the formation of new intermetallic phases between Sn and Zr is possible. However, detailed EDS and XRD analyses show that α-Mg and Mg_2Sn are the only constituents in the as-cast Mg–5Sn alloy and addition of 1 wt% Zr does not cause the formation of any new phases such as

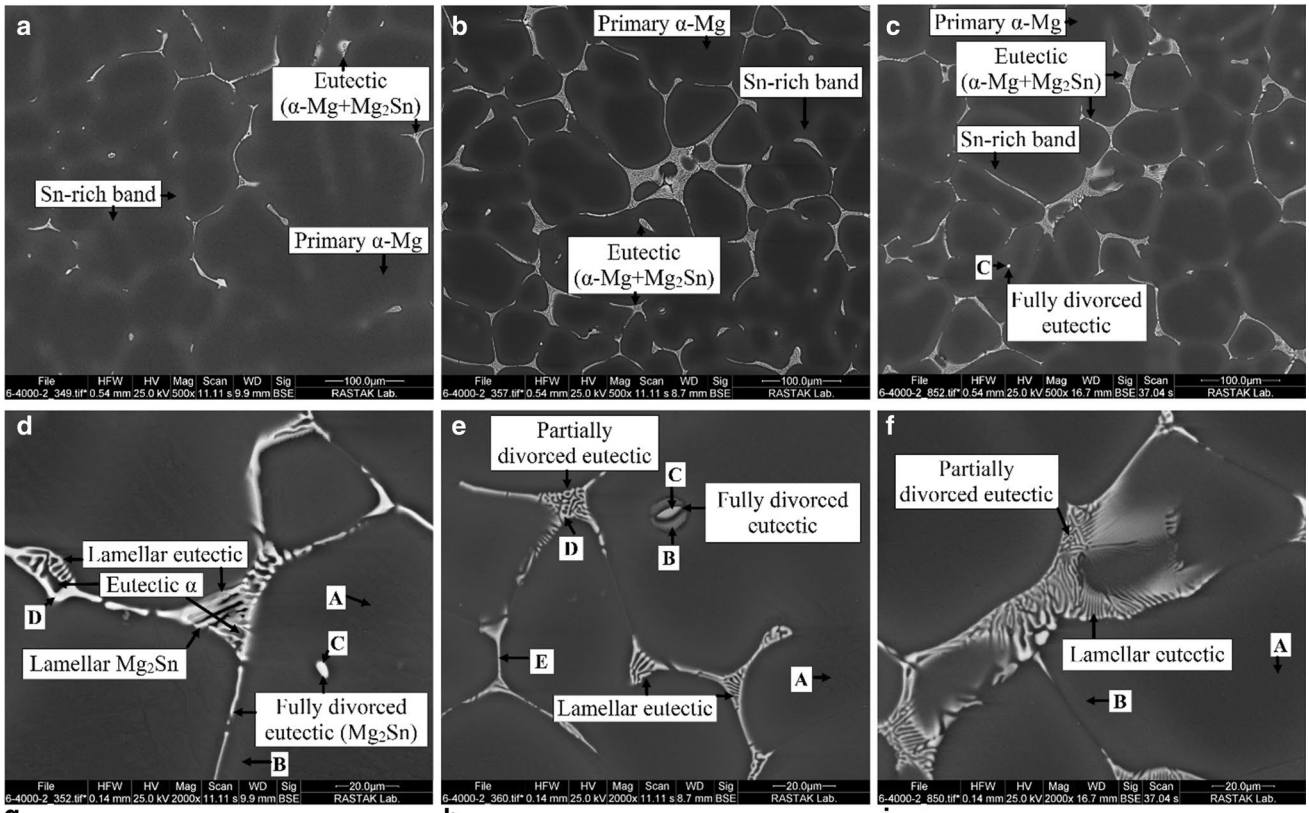

g

Position	Element (at.%)		
	Mg	Sn	Zr
A	99.54	0.46	-
B	97.85	2.15	-
C	86.72	13.28	-
D	76.18	23.82	-

h

Position	Element (at.%)		
	Mg	Sn	Zr
A	99.40	0.59	0.01
B	96.22	3.71	0.07
C	90.50	9.33	0.17
D	88.34	11.60	0.06
E	86.93	12.98	0.09

i

Position	Element (at.%)		
	Mg	Sn	Zr
A	99.21	0.66	0.13
B	97.83	1.94	0.23
C	86.84	12.69	0.47

Fig. 4 SEM micrographs of as-cast **a**, **d** Mg–5Sn, **b**, **e** Mg–5Sn–0.5Zr and **c**, **f** Mg–5Sn–1Zr alloys together with their corresponding EDS analysis results

Sn_2Zr. In general, the ability of two elements in forming intermetallic compounds is proportional to their electronegative difference [43]. The electronegative values of Mg, Sn and Zr are 1.31, 1.96 and 1.33, respectively. Therefore, the formation of the Sn_2Zr compound is relatively more difficult than the Mg_2Sn phase. Our results are in agreement with those reported by Yang et al. [29, 30] who reported that the Sn_2Zr phase appeared in Mg–Sn based alloys when Zr content exceeded 1.18 wt%. From XRD analysis results presented in Fig. 3, it can be observed that the intensity of diffraction peaks of the Mg_2Sn phase increases with increasing Zr content of the alloys. These results are in accord with the microstructural observations (Fig. 4), which show that the volume fraction of the Mg_2Sn precipitates increases with Zr addition. This is especially obvious when Zr content increases from 0 to 0.5 wt%, indicating that Zr probably facilitates the heterogeneous nucleation of Mg_2Sn precipitates. In addition, Zr addition may decrease the solid solubility of Sn in Mg, enhancing the driving force for the formation of Mg_2Sn precipitates.

Figure 5 shows the microstructures of as-homogenized alloys. Neither the bright Sn-rich band nor the eutectic structure is observed in the microstructure of as-homogenized binary Mg–5Sn alloy, as shown in Fig. 5a. The XRD results presented in Fig. 3 reveal the disappearance of Mg_2Sn diffraction peaks of the Mg–5Sn alloy after homogenization, indicating that Mg_2Sn precipitates have been dissolved in the α-Mg matrix. In contrast, the same homogenization treatment does not dissolve all the Mg_2Sn phase existed in the Zr-containing alloys. As can be seen in Fig. 5c, the amount of remnant Mg_2Sn phase in the microstructure of as-homogenized Mg–5Sn–1Zr alloy is substantial. The detection of Mg_2Sn diffraction peaks in the XRD pattern of as-homogenized Mg–5Sn–1Zr alloy in Fig. 3 confirms these microstructural observations. In general, dissolution is a diffusion-associated process and thus depends on the

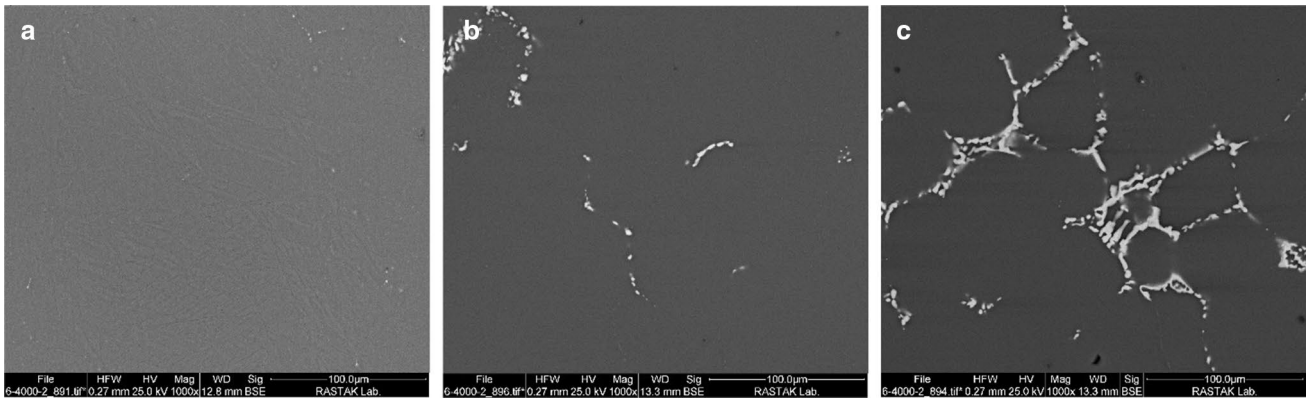

Fig. 5 SEM micrographs of as-homogenized **a** Mg–5Sn, **b** Mg–5Sn–0.5Zr and **c** Mg–5Sn–1Zr alloys

time and temperature at which the treatment is carried out. At a constant annealing temperature, the Mg–5Sn–1Zr alloy with a higher volume fraction of the second phase needs a more extended heating period for the complete dissolution of the Mg_2Sn phase. These results indicate that the thermal stability of the binary Mg–Sn alloys is increased by Zr addition. The superior microstructural stability of Zr-containing Mg–Sn alloys can also be attributed to the probable hindering effect of Zr on the diffusion of Sn atoms within the α-Mg matrix.

The microstructures of extruded Mg–5Sn and Mg–5Sn–1Zr alloys, as exhibited in Fig. 6, consists of the equiaxed grain of α-Mg with fine and coarse precipitates of Mg_2Sn. Fine Mg_2Sn particles are less than 2 μm in size and have been reprecipitated during hot extrusion at both grain boundaries and grain interiors. Sn solute atoms that

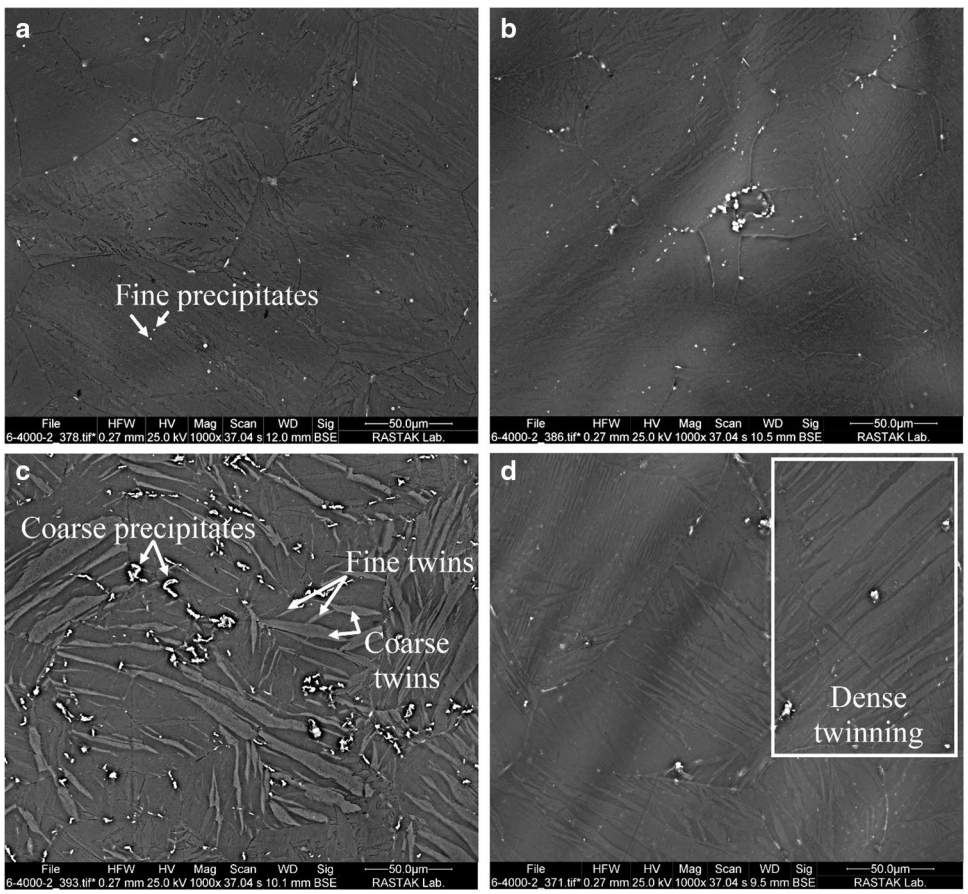

Fig. 6 SEM micrographs of as-extruded **a**, **b** Mg–5Sn and **c**, **d** Mg–5Sn–1Zr alloys with extrusion ratio of **a**, **c** 6 and **b**, **d** 12

Table 1 The average grain size (in μm) of the as-cast and extruded alloys

Alloy	As-cast	ER6	ER12
Mg–5Sn	211	38	45
Mg–5Sn–0.5Zr	145	36	39
Mg–5Sn–1Zr	107	34	35

are dissolved in the α-Mg matrix during homogenization can re-form fine Mg_2Sn particles through dynamic precipitation. From the binary Mg–Sn phase diagram, Mg_2Sn precipitates can form in the Mg–5Sn alloy at temperatures lower than 420 °C [5]. Therefore, the precipitation of Mg_2Sn particles during extrusion at 400 °C is anticipated. Coarse Mg_2Sn particles, which are mostly observed in the Mg–5Sn–1Zr alloy, are caused by fragmentation of large eutectic phases, remained from homogenizing treatment along grain boundaries.

In comparison to the as-cast samples, the grain size of the extruded alloys is refined, as reported in Table 1. After extrusion with the area-reduction ratio of 6, the average grain size of the Mg–5Sn and Mg–5Sn–1Zr alloys was calculated as 38 and 34 μm, respectively, which are much finer than their corresponding value in the as-cast condition. This grain refinement can be attributed to the dynamic recrystallization (DRX), as observed in the microstructure of extruded alloys shown in Fig. 6. It is revealed that the extruded alloys exhibit a bimodal microstructure consisting of relatively coarse and fine grains. Deformation twins are noticed within the relatively coarse grains.

Twin dynamic recrystallization (TDRX), which was found to be unique to Mg and its alloys, can be the predominant DRX mechanism at low plastic strains, high strain rates and low to intermediate deformation temperatures (20–350 °C) [44, 45]. However, there are reports confirming that twinning still plays an important role in DRX of Mg alloys at elevated temperatures [46]. Twinning interfaces and original grain boundaries provide additional sites for nucleation of recrystallized grains in Mg alloys [47]. Due to the restricted numbers of slip systems, characteristic of the HCP crystal structure, and coarse microstructure of the alloys, many twins appear in the original grains. Several twins can be identified within a deformed original grain, most of which are parallel to each other. Locally, fine twins are limited by coarse twins. In fact, the twinning formation has divided the original grains into smaller segments. It seems in this situation that deformation is proceeded by the growth of existing twins, and consequently, DRX and grain refinement are achieved by the succession of twinning. This type of twin-assisted DRX is in good agreement with previous reports for AZ series of Mg alloys [48, 49]. The accumulation of distortion energy by twining is considered as the reason for the TDRX [50]. Therefore, increasing the extrusion ratio from 6 to 12 results in the formation of a dense twinning zone as shown for the Mg–5Sn–1Zr alloy in Fig. 6d. In addition, some fine grains are observed around coarse particles in the microstructure of extruded Zr-containing alloys, as shown in Fig. 6c. This is related to the particle-stimulated nucleation (PSN) [51].

Regardless of the Zr content of the alloy, ER12 samples show a slightly coarser grain size in comparison to ER6 ones, but the difference becomes smaller as the Zr content increases. Extrusion at a higher ratio in a constant ram speed results in a larger total strain, which reduces the recrystallization temperature [26]. Therefore, at a constant extrusion temperature, a higher degree of grain growth is expected for extrusion at a higher ratio. In addition, a higher extrusion ratio at a constant ram speed corresponds to a higher extrusion velocity. This can raise the die exit temperature, leading to a relatively larger grain size [47]. As the material exits the extrusion die and cools to room temperature, some degree of grain coarsening may also occur through the metadynamic recrystallization (MDRX) mechanism. The increase in grain size due to MDRX is effectively reduced by Zr addition in Mg alloys [52]. This could be the reason why the influence of the extrusion ratio on the final grain size is reduced with increasing Zr content.

3.2 Mechanical Properties

Typical Engineering stress-strain curves of Mg–5Sn–xZr alloys tested at room temperature are presented in Fig. 7. The results of tensile tests, including yield strength (YS), ultimate tensile strength (UTS) and elongation to fracture (e_f) are summarized in Table 2. As observed, both strength

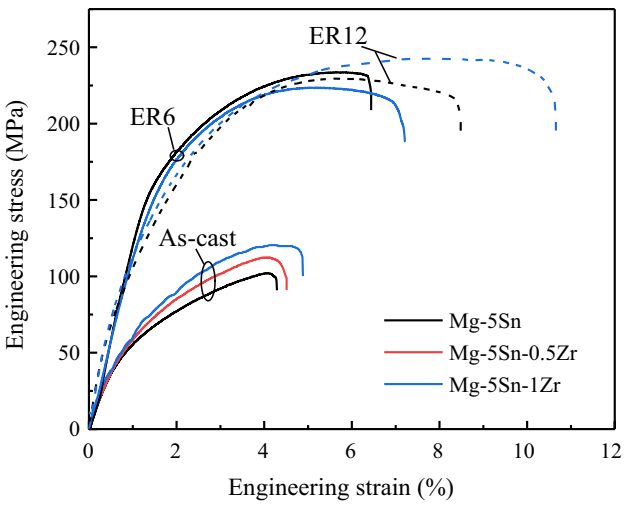

Fig. 7 Engineering stress–strain curves of as-cast and extruded Mg–5Sn–xZr alloys

Table 2 Tensile properties of as-cast and extruded Mg–5Sn–xZr alloys

Alloy	YS (MPa)			UTS (MPa)			e_f (%)		
	As-cast	ER6	ER12	As-cast	ER6	ER12	As-cast	ER6	ER12
Mg–5Sn	52	148	121	101	234	230	4.3	6.4	8.4
Mg–5Sn–0.5Zr	57	145	128	112	229	234	4.5	6.8	9.1
Mg–5Sn–1Zr	61	142	125	119	223	243	4.9	7.1	10.6

and ductility of the Mg–5Sn alloy in the as-cast condition increase with Zr addition. The as-cast Mg–5Sn alloy exhibited a yield strength of 52 MPa, which was increased 17% by the addition of 1 wt% Zr. The grain refinement and increased fraction of Mg_2Sn precipitates with Zr addition are the main strengthening reasons. The small improvement in elongation with Zr addition can also be attributed to the as-cast microstructural change from dendritic morphology to the nearly globular type.

According to Table 2, both strength and ductility of the alloys are significantly improved after hot extrusion. This is due to the obvious grain refinement and formation of fine Mg_2Sn dispersoids caused by DRX and dynamic precipitation during the hot extrusion. The strengthening contribution of grain boundaries presented by the well-known Hall–Petch relation is substantial for HCP metals such as Mg with a restricted number of slip planes. In addition, the coarse dendritic structure with large Mg_2Sn intermetallic compounds in the dendrite/grain boundaries, as those observed for the as-cast alloys, promote initiation and propagation of cracks under tensile loads, leading to a reduction in strength and ductility.

The presence of deformation twins in the extruded alloys has a substantial effect on mechanical properties. Twin boundaries act as an obstacle to dislocation motion, and similar to grain boundaries are effective at dislocations trapping. In some reports on Mg alloys [53], the contribution of twinning in flow stress exceeded the effect of grain size. However, assuming twin boundaries sub-divide a grain into smaller grains, the Hall–Petch equation has been used to evaluate the strengthening contribution of twins [54, 55]. As with other Mg alloys, hot extruded Mg–Sn based alloys exhibit fiber texture [26], which also enhances the strength of the extruded alloys. On the other hand, twins can accommodate more strains compared to the matrix. Therefore, they locally relieve the applied tensile stress leading to an increased ductility [53].

The effect of extrusion ratio on the tensile properties was observed to be rather complicated. As shown in Table 2, the yield strength decreases with an increase of extrusion ratio from 6 to 12, regardless of the Zr content of the alloy. As described earlier, the grain size of Mg–5Sn–xZr alloys become relatively larger with increasing extrusion ratio. Besides, a higher degree of deformation, i.e. higher extrusion ratio, results in a relatively weaker texture [26, 47]. Therefore, a reduction in yield strength with an increase of extrusion ratio from 6 to 12 is expected.

At a constant extrusion ratio, the yield strength was not observed to change obviously with Zr addition. Almost similar values of yield and tensile strength were observed for the alloys containing different Zr contents. In addition, tensile strength did not considerably change with the extrusion ratio. Though, there is an exception for the Mg–5Sn–1Zr alloy, which revealed the lowest increase in grain size with increasing extrusion ratio. The tensile strength of the Mg–5Sn–1Zr alloy increases from 223 to 243 MPa, as the extrusion ration increases from 6 to 12. The lower tensile strength of the ER6 sample is attributed to the presence of coarse Mg_2Sn precipitates within the matrix of Mg–5Sn–1Zr alloy, as exhibited in Fig. 6c. These coarse particles are not observed in the microstructure of the alloy extruded at the ratio of 12 (Fig. 6d), which is strengthened by finer particles. A higher degree of deformation caused by a higher extrusion ratio breaks the coarse precipitates that remained from the homogenizing treatment more effectively. Therefore, the alloy matrix is strengthened by the presence of finer particles that pin mobile dislocations strongly. The highest tensile strength (243 MPa) that is obtained for the Mg–5Sn–1Zr alloy extruded with the ratio of 12 suggests that fine particles can play an important role in strain hardening response of Mg alloys.

To further clarify the hardening response of the alloys at different conditions, studying the hardening capacity and strain hardening rates obtained from tension tests is beneficial. Hardening capacity, H_c, of a material may be defined as [56, 57]:

$$H_c = \frac{\sigma_{UTS} - \sigma_{YS}}{\sigma_{YS}} = \frac{\sigma_{UTS}}{\sigma_{YS}} - 1 \quad (1)$$

Figure 8 shows the calculated H_c values of Mg–5Sn–xZr alloys at various conditions. It is observed that Zr addition does not significantly change the hardening capacity, regardless of the alloy condition. For all the alloys, the lowest H_c value was obtained in ER6 condition, which could be attributed to its smaller grain size. A reduction in grain size would decrease dislocation storage ability, leading to the lower hardening capacity [57, 58].

Figure 9 illustrates the strain hardening rate ($\theta = d\sigma/d\varepsilon$) versus the net flow stress ($\sigma - \sigma_y$) of the alloys in different

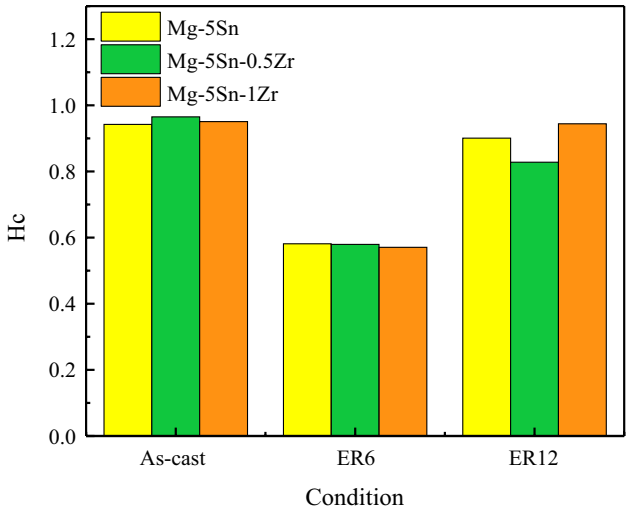

Fig. 8 Calculated hardening capacities of Mg–5Sn–xZr alloys at various conditions

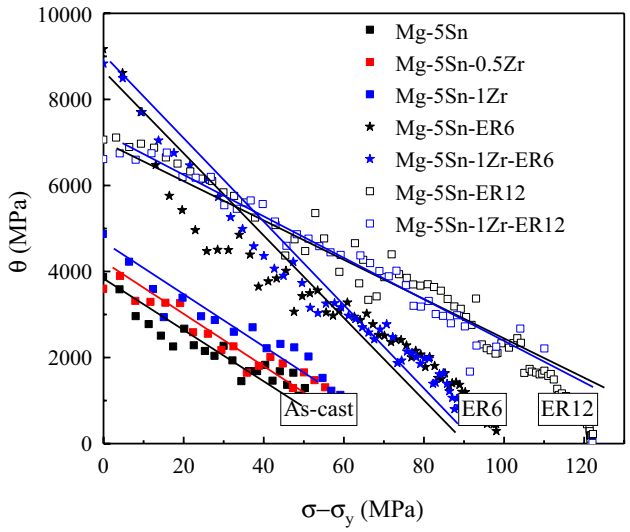

Fig. 9 Strain hardening rate versus net flow stress for the as-cast and extruded alloys

conditions, where σ and ε are true stress and true strain, respectively. It is found for all the samples that the strain hardening rate linearly decreases with net flow stress, exhibiting stage III (parabolic) hardening behavior. Compared with extruded alloys, the as-cast alloys show lower strain hardening rates due to their larger grain size. The grain refinement and increased volume fraction of Mg_2Sn precipitates with Zr addition in the as-cast alloys raised the strain hardening rate. In extruded condition, the ER6 samples exhibited higher initial strain hardening rates than the ER12 samples. At higher net flow stress levels, this was reversed. The initially higher strain hardening rates of ER6 alloys can be attributed to their smaller grain size. However, the contribution of grain size in strain hardening rate diminishes at higher strains because of dislocation screening and dynamic recovery at grain boundaries [58]. At higher flow stresses, the strain hardening of materials is more associated with the motion of dislocation by slip and their interactions. Therefore, the enhanced strain hardening rate of ER12 samples at higher flow stresses should be sought in microstructural characteristics that hinder slip of dislocations. Twins refine the grains and act as barriers to dislocation movement, thereby reduce the effective slip distance of dislocation and increase the work hardening rate [59]. Besides, the presence of dispersive and finer Mg_2Sn precipitates in ER12 samples can drastically decrease dislocation mean free path, leading to a higher strain hardening rate.

As for ductility, a significant improvement in elongation to failure was realized as the extrusion ratio increased. The Mg–5Sn–1Zr alloy with the extrusion ratio of 12 exhibits the highest tensile elongation (~ 10.6%). The ductility of materials is generally associated with the initiation and propagation of cracks. A higher deformation level, which is involved in the extrusion with a higher ratio, hinders the crack nucleation and growth during the subsequent deformation. The greater hardening capacities of ER12 samples compared with those of ER6 alloys led to higher elongations. Meanwhile, it is not easy for voids to nucleate at the interface of fine (< 2.5 μm) strengthening particles present in the microstructure of ER12 samples due to their better bonding with the matrix [60]. Additionally, a comparatively strong basal texture that forms at the lower extrusion ratio results in a relatively low tensile elongation value [47]. Hence, an increase either in the Zr content or the extrusion ratio results in ductility enhancement.

SEM micrographs of tensile fracture surfaces of as-cast and extruded alloys are shown in Fig. 10. The addition of Zr exhibits a negligible influence on the appearance of the fracture surface in the as-cast condition. Meanwhile, there was found to be substantial differences in the appearance of fracture surfaces of the alloys in as-cast and extruded conditions. The fracture surfaces of the as-cast alloys shown in Fig. 10a, b are mainly composed of large cleavage-type facets, characteristics of obvious cleavage fracture mode. Elongated parallel grooves, characteristics of the fluting fracture are also observed in the Mg matrix of the alloys. However, the most marked aspect of these surfaces is the formation of large secondary cracks. These cracks are observed within the eutectic structures or along the interface between the α-Mg matrix and the eutectic phase. The primary reason for crack formation is the microstructural inhomogeneity causing local stress raisers. Coarse Mg_2Sn compounds, distributed along dendrite/grain boundaries of the as-cast alloy, are complex in shape and provide appropriate sites for

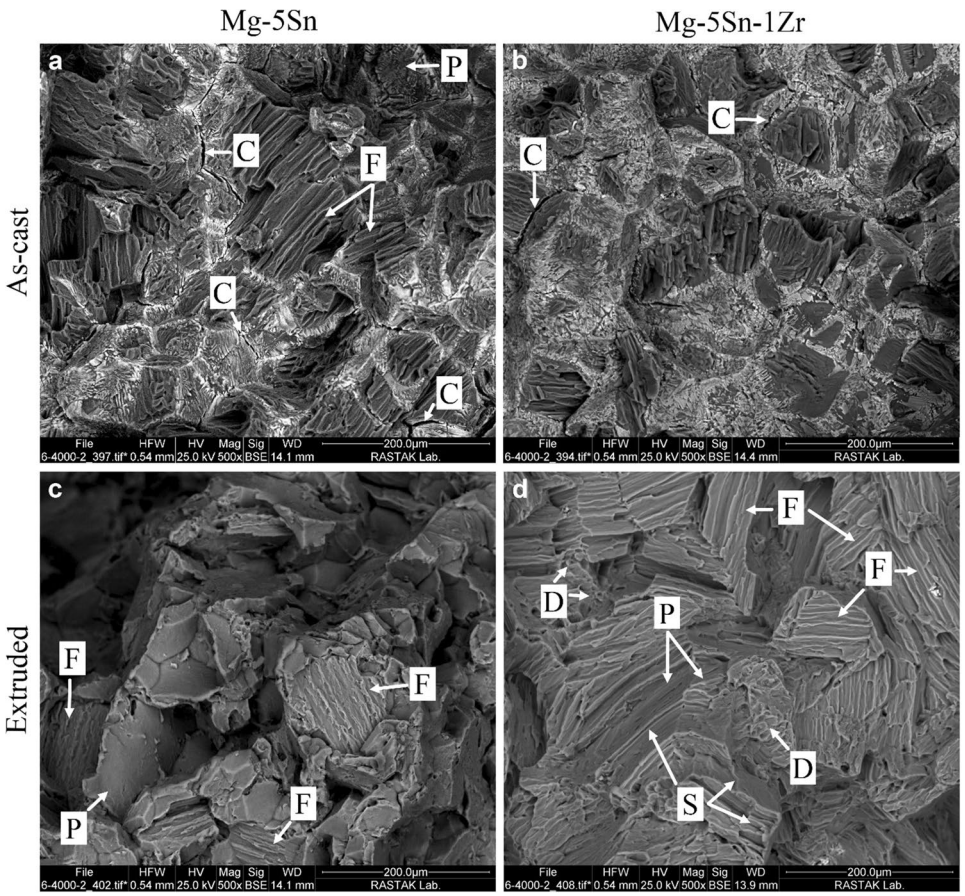

Fig. 10 SEM micrographs of the fracture surface after tensile tests for **a** as-cast Mg–5Sn, **b** as-cast Mg–5Sn–1Zr, **c** Mg–5Sn–ER6 and **d** Mg–5Sn–1Zr–ER12 alloys (C: secondary cracks, D: dimples, F: flutes, P: cleavage planes or facets, S: cleavage steps)

local stress concentration. Therefore, large secondary cracks are found to nucleate and propagate in the interdendritic regions. As a result, the fracture is of intergranular type, which results in the reduced strength and limited ductility of the as-cast alloy, as reported in Table 2.

The fracture surfaces of extruded alloys (Fig. 10c, d) reveals evidence of microstructural uniformity. The observed twins retard the initiation and propagation of cracks during the fracture process through enhancing the plastic dissipation in the matrix and accommodating the strain incompatibility [61]. Since the interdendritic eutectic structures do not exist in the extruded alloys, the applied tensile stresses are accumulated on cleavage planes, causing a transition to transgranular fracture. Compared to the as-cast alloy, the fracture surface of extruded alloys is rougher and shows a higher degree of plastic deformation. A higher density of flutes that are a result of a plastic deformation process [62] is evident in the fracture surface of the extruded alloys. In addition, the area of fluting region increases with Zr addition. Tear ridges are also realized around the upper surface of flutes. However, a large number of cleavage planes are again observed in the fracture surface. Some cleavage steps can be noticed, which join cleavage planes formed at different altitudes. The network of cleavage steps has created river patterns. Fine-scale dimples, as well as large cleavage facets and steps, are observed in the fracture surface of Mg–5Sn–1Zr alloy with the extrusion ratio of 12, as exhibited in Fig. 10d. Therefore, extruded alloys show characteristics of quasi-cleavage fracture as the dominant fracture mode.

Figure 11 illustrates the hardness variations with the Zr content of the alloys. The hardness of the as-cast Mg–5Sn alloy is slightly improved with Zr addition. A significant increase in the volume fraction of the Mg_2Sn compound with Zr addition is responsible for the observed hardness improvement. Mg_2Sn is a hard and brittle phase with a hardness of about 119 HV [4, 63], thereby contributes to the hardening of the soft α-Mg matrix. The hardness of extruded alloys does not change significantly with Zr addition. However, the hardness of all the alloys increased significantly after hot extrusion, which can be ascribed to the hardening mechanisms discussed previously. The effect of the extrusion ratio on the hardness of the alloys is also negligible.

4 Conclusion

Microstructure and mechanical properties of the as-cast and extruded Mg–5Sn–xZr alloys are studied. The main conclusions can be summarized as follows:

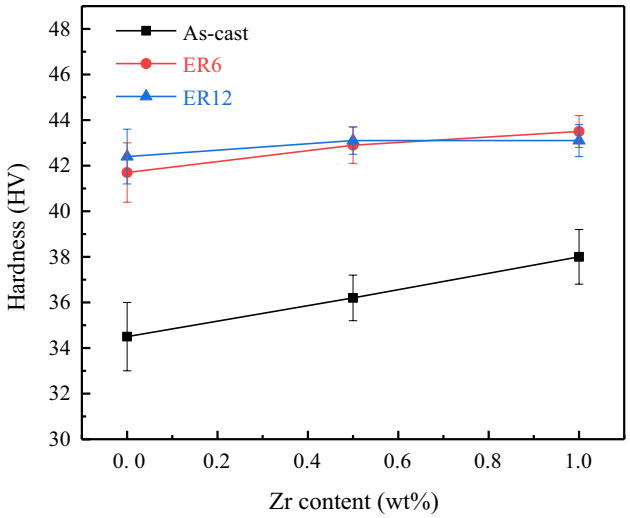

Fig. 11 Vickers hardness of the as-cast and extruded Mg–5Sn–xZr alloys

1. The as-cast microstructure of the alloys consists of α-Mg and Mg_2Sn phases. A transition from dendritic to nearly globular structure was observed with Zr addition. Besides, substantial grain refinement is noticed in Zr-containing alloys.
2. Different types of eutectic morphologies, including lamellar, fully divorced, and partially divorced structures are observed in the Mg–Sn–Zr system. The overall volume fraction of the eutectic phase and the tendency to form partially divorced eutectic increases with an increase in Zr content of the alloy.
3. Zr enhances the microstructural stability of the Mg–5Sn alloy during homogenizing treatment at high temperatures.
4. The microstructure significantly changes after the hot extrusion. These changes include grain refinement through twin-assisted DRX, fragmentation of coarse Mg_2Sn phase and dynamic precipitation of fine Mg_2Sn particles. As-extruded samples exhibited greater strain hardening rates compared with the as-cast alloys. An increase in the extrusion ratio from 6 to 12 resulted in slightly coarser grains, which in turn reduced the yield strength and increased strain hardening capacity of the alloys.
5. Optimum strength and ductility are obtained in the Mg–5Sn–1Zr alloy extruded with the area-reduction ratio of 12. The yield strength, tensile strength and elongation to failure of this alloy are measured as 125 MPa, 243 MPa, and 10.6%, respectively.
6. The microstructures of as-cast alloys are prone to intergranular fracture under tensile stresses, deteriorating their strength and ductility. However, the fracture surfaces of extruded alloys are characterized by cleavage facets and steps together with extensive fluting and local dimples, indicating that quasi-cleavage is the dominant fracture mode.

Funding No funding was received for conducting this study.

Compliance with Ethical Standards

Conflict of interest The authors declare that they have no conflict of interest.

Ethical Approval This article does not contain any studies with human participants or animals performed by any of the authors.

References

1. A. Dev, M. Paliwal, J. Cryst. Growth **503**, 28–35 (2018)
2. B.Q. Shi, R.S. Chen, W. Ke, J. Alloy. Compd. **509**, 3357–3362 (2011)
3. A. Gökçe, Met. Mater. Int. **26**, 1036–1044 (2020)
4. H. Liu, Y. Chen, Y. Tang, S. Wei, G. Niu, J. Alloy. Compd. **440**, 122–126 (2007)
5. N. Hort, Y. Huang, T. Abu Leil, P. Maier, K.U. Kainer, Adv. Eng. Mater. **8**, 359–364 (2006)
6. P. Poddar, K.L. Sahoo, Mater. Sci. Eng. A **556**, 891–905 (2012)
7. F.R. Elsayed, T.T. Sasaki, C.L. Mendis, T. Ohkubo, K. Hono, Mater. Sci. Eng. A **566**, 22–29 (2013)
8. A.A. Nayeb-Hashemi, J.B. Clark, Bull. Alloy Phase Diagr. **5**, 466–476 (1984)
9. M. Cong, Z. Li, J. Liu, X. Miao, B. Wang, Q. Xi, Russ. J. Non-Ferr. Met. **57**, 445–455 (2016)
10. C.L. Mendis, K. Hono, *Fundamentals of Magnesium Alloy Metallurgy* (Woodhead Publishing, Sawston, 2013), pp. 125–151
11. C.L. Mendis, C.J. Bettles, M.A. Gibson, C.R. Hutchinson, Mater. Sci. Eng. A **435–436**, 163–171 (2006)
12. Y. Huang, H. Dieringa, K.U. Kainer, N. Hort, Fatigue Fract. Eng. M. **36**, 308–315 (2013)
13. Y. Jiang, Y.A. Chen, D. Fang, L. Jin, Mater. Sci. Eng. A **641**, 256–262 (2015)
14. H. Liu, Y. Chen, H. Zhao, S. Wei, W. Gao, J. Alloy. Compd. **504**, 345–350 (2010)
15. G. Nayyeri, R. Mahmudi, Mater. Sci. Eng. A **527**, 669–678 (2010)
16. E. Karakulak, Y.B. Küçüker, J. Magn. Alloys **6**, 384–389 (2018)
17. J. Jiang, G. Bi, J. Liu, C. Ye, J. Lian, Z. Jiang, J. Magn. Alloys **2**, 257–264 (2014)
18. X.Y. Qian, Y. Zeng, B. Jiang, Q.R. Yang, Y.J. Wan, G.F. Quan, F.S. Pan, J. Alloy. Compd. **820**, 153122 (2020)
19. G. Yarkadaş, L.C. Kumruoğlu, H. Şevik, Mater. Charact. **136**, 152–156 (2018)
20. H.-D. Zhao, G.-W. Qin, Y.-P. Ren, W.-L. Pei, D. Chen, Y. Guo, T. Nonferr. Metal. Soc. **20**, s493–s497 (2010)
21. P. Poddar, S. Bagui, K. Ashok, A.P. Murugesan, J. Alloy. Compd. **695**, 895–908 (2017)
22. T.T. Sasaki, K. Yamamoto, T. Honma, S. Kamado, K. Hono, Scripta Mater. **59**, 1111–1114 (2008)
23. Z. Zeng, N. Stanford, C.H.J. Davies, J.-F. Nie, N. Birbilis, Int. Mater. Rev. **64**, 27–62 (2019)
24. T. Homma, N. Kunito, S. Kamado, Scripta Mater. **61**, 644–647 (2009)

25. N. El Mahallawy, A. Ahmed Diaa, M. Akdesir, H. Palkowski, Mater. Sci. Eng. A **680**, 47–53 (2017)
26. Y. Zhang, X.-Y. Chen, Y.-L. Lu, X.-P. Li, T. Nonferr. Metal. Soc. **28**, 2190–2198 (2018)
27. I.J. Polmear, *Light Alloys*, 4th edn. (Butterworth-Heinemann, Sawston, 2005), pp. 237–297
28. E.F. Emley, *Principles of Magnesium Technology* (Pergamon, Oxford, New York, 1996)
29. F. Pan, M. Yang, Mater. Sci. Eng. A **528**, 4973–4981 (2011)
30. M. Yang, X. Liang, Z. Yi, F. Pan, Mater. Design **32**, 1967–1973 (2011)
31. M.C. Flemings, Metall. Trans. **5**, 2121–2134 (1974)
32. M.A. Easton, D.H. StJohn, Acta Mater. **49**, 1867–1878 (2001)
33. J.W. Fu, Y.S. Yang, J. Cryst. Growth **322**, 84–90 (2011)
34. M. Qian, D.H. Stjohn, Int. J. Cast Met. Res. **22**, 256–259 (2009)
35. Y. Ali, D. Qiu, B. Jiang, F. Pan, M.-X. Zhang, J. Alloy. Compd. **619**, 639–651 (2015)
36. E. Karakulak, J. Magn. Alloys **7**, 355–369 (2019)
37. Y.C. Lee, A.K. Dahle, D.H. StJohn, Metall. Mater. Trans. A **31**, 2895–2906 (2000)
38. D.H. StJohn, M. Qian, M.A. Easton, P. Cao, Z. Hildebrand, Metall. Mater. Trans. A **36**, 1669–1679 (2005)
39. M. Qian, D.H. StJohn, M.T. Frost, Mater. Sci. Forum **419–422**, 593–598 (2003)
40. M. Keyvani, R. Mahmudi, G. Nayyeri, Mater. Sci. Eng. A **527**, 7714–7718 (2010)
41. D.M. Stefanescu, *Science and Engineering of Casting Solidification*, 2nd edn. (Springer US, Berlin, 2009), pp. 1–52
42. A.K. Dahle, Y.C. Lee, M.D. Nave, P.L. Schaffer, D.H. StJohn, J. Light Met. **1**, 61–72 (2001)
43. H. Liu, Y. Chen, Y. Tang, D. Huang, G. Niu, Mater. Sci. Eng. A **437**, 348–355 (2006)
44. R. Kaibyshev, *Advances in Wrought Magnesium Alloys* (Woodhead Publishing, Sawston, 2012), pp. 186–225
45. O. Sitdikov, R. Kaibyshev, Mater. Trans. **42**, 1928–1937 (2001)
46. Q. Ma, B. Li, E.B. Marin, S.J. Horstemeyer, Scripta Mater. **65**, 823–826 (2011)
47. M. Shahzad, L. Wagner, Mater. Sci. Eng. A **506**, 141–147 (2009)
48. M.M. Myshlyaev, H.J. McQueen, A. Mwembela, E. Konopleva, Mater. Sci. Eng. A **337**, 121–133 (2002)
49. S.W. Xu, N. Matsumoto, S. Kamado, T. Honma, Y. Kojima, Scripta Mater. **61**, 249–252 (2009)
50. A. Malik, Y. Wang, C. Huanwu, F. Nazeer, B. Ahmed, M.A. Khan, W. Mingjun, Mater. Sci. Eng. A **771**, 138649 (2020)
51. J.D. Robson, D.T. Henry, B. Davis, Acta Mater. **57**, 2739–2747 (2009)
52. A.G. Beer, *Advances in Wrought Magnesium Alloys*, 1st edn. (Woodhead Publishing, Sawston, 2012), pp. 304–322
53. L. Jiang, J.J. Jonas, R.K. Mishra, A.A. Luo, A.K. Sachdev, S. Godet, Acta Mater. **55**, 3899–3910 (2007)
54. H. Somekawa, T. Mukai, Mater. Sci. Eng. A **561**, 378–385 (2013)
55. M. Schneider, E.P. George, T.J. Manescau, T. Záležák, J. Hunfeld, A. Dlouhý, G. Eggeler, G. Laplanche, Int. J. Plast. **124**, 155–169 (2020)
56. N. Afrin, D.L. Chen, X. Cao, M. Jahazi, Scripta Mater. **57**, 1004–1007 (2007)
57. L. Zhang, K.-K. Deng, K.-B. Nie, F.-J. Xu, K. Su, W. Liang, Mater. Sci. Eng. A **636**, 279–288 (2015)
58. S.M. Chowdhury, D.L. Chen, S.D. Bhole, X. Cao, E. Powidajko, D.C. Weckman, Y. Zhou, Mater. Sci. Eng. A **527**, 2951–2961 (2010)
59. B. Wang, R. Xin, G. Huang, Q. Liu, Mater. Sci. Eng. A **534**, 588–593 (2012)
60. M. Moazami-Goudarzi, F. Akhlaghi, Tribol. Int. **102**, 28–37 (2016)
61. N.S. Prasad, N. Naveen Kumar, R. Narasimhan, S. Suwas, Acta Mater. **94**, 281–293 (2015)
62. ASM International, *ASM Handbook, Fractography*, vol. 12 (ASM International, Cleveland, 1992)
63. R.G. Guan, Y.F. Shen, Z.Y. Zhao, R.D.K. Misra, Sci. Rep. **6**, 23154 (2016)